Machine learning to probe modal interaction in dynamic atomic force microscopy

Belardinelli, P.; Chandrashekar, A.; Wiebe, R.; Alijani, F.; Lenci, S.

Important note
To cite this publication, please use the final published version (if applicable).
Please check the document version above.

Machine learning to probe modal interaction in dynamic atomic force microscopy

P. Belardinelli [a],*, A. Chandrashekar [b], R. Wiebe [c], F. Alijani [b], S. Lenci [a]

[a] *Department of Construction, Civil Engineering and Architecture, Polytechnic University of Marche, Ancona, Italy*
[b] *Department of Precision and Microsystems Engineering, Delft University of Technology, Mekelweg 2, 2628CD, Delft, The Netherlands*
[c] *Department of Civil and Environmental Engineering, University of Washington, Seattle, WA, 98195-2400, USA*

ARTICLE INFO

ABSTRACT

Modal interactions are pervasive effects that commonly emerge in nanomechanical systems. The coupling of vibrating modes can be leveraged in many ways, including to enhance sensing or to disclose complex phenomenologies. In this work we show how machine learning and data-driven approaches could be used to capture intermodal coupling. We employ a quasi-recurrent neural network (QRNN) for identifying mode coupling and verify its applicability on experimental data obtained from tapping mode atomic force microscopy (AFM). Hidden units of the QRNN are monitored to trace fingerprints of modes activation and to quantify their contributions over the global distortion of orbits in the phase space. To demonstrate the broad applicability of the method, the trained model is re-applied over different experiments and on diverse materials. Over a range of tip-sample configurations, dynamic AFM possesses features general enough to be seized by the QRNN and it is not required an ad-hoc re-training for the identification of interacting modes. Our study opens up a route for utilizing established machine learning techniques for rapid recognition of nonlinear complex effect such as internal resonances in nanotechnology. The QRNN analysis is meant to assist AFM sensing operations when exploiting modal interaction to enhance the signal-to-noise ratio of higher harmonics and provide high resolution compositional contrast in multi-frequency AFM applications.

1. Introduction

Nanomechanical systems lie in a playground where the linear behavior is an exception [1,2]. Nonlinearities give rise to interesting phenomena which have the potential to be valorized into innovative nanomechanical sensors and novel detection schemes [3–6]. Engineering of nonlinearities specifically find applications in detection of weak forces [7,8], employed in signal amplification and noise-squeezing effect [9,10], phase-sensitive mechanical amplifiers to leverage the sensitivity in mass measurement [11,12].

The study of nonlinear dynamics at the nanoscale has recently grabbed attention within the realm of dynamic atomic force microscopy (AFM) [13,14]. Dynamic AFM is a non-destructive, nanoscale technique utilized for characterizing synthetic and biological matter. In this technique, a force-sensing resonant microcantilever with a sharp tip at its free end (Fig. 1(a)) probes the topography and other nanomechanical properties of the sample surface [15]. The highly nonlinear nature of tip-sample interaction emanates coupling between vibrational modes even if in far apart frequency range [16,17] that thrive due to internal resonances, a condition where the ratio between two or more resonance frequencies of the cantilever is a rational number [18]. Higher modes of vibration intervene in the oscillatory behavior of the AFM microcantilever. The resulting complex motion could be exploited

for enhancing the sensitivity and accuracy of AFM characterization techniques [14,19,20]. Nevertheless, to date only a handful of studies have actually looked into nonlinear phenomena of AFM and to undiscovered improvements in tapping operational mode. Since the standard feedback-control loop of the AFM controller works upon a homodyne detection scheme, it automatically masks all the higher order spectral components. Circumventing the issue means to bypass the controller and to collect the raw deflection signal directly from the AFM photo-detector. A field-programmable gated array (FPGA) is capable of this, and it retrieves all the signatures indicative of the rich nonlinear interplay within the tip and the sample, even allowing to reconstruct the actual instantaneous interaction force [21].

However, in order to determine higher vibrational components in the time and frequency domain, the signal must be collected at very high frame rate for relatively long duration in order to minimize spectral leakage with the use of suitable windowing methods. This means to collect millions of data points which is an enormous ordeal in the data handling and post processing. Moreover, a simple inspection of mode coupling is challenging since the higher order modes have smaller amplitudes and are often buried under the noise floor. It is clear that, in such conditions, new detection schemes based on nonlinear modes coupling lose practical applicability. Here, it is where machine learning (ML) techniques may provide overwhelming benefits.

ML-augmented approaches have revolutionized the analysis and the understanding of complex data, recognizing patterns, and developing classifications based on multimodal datasets in various situations otherwise inexplicable [22]. Recently, sparse identification methods and symbolic regression have made giant strides in their predictive capabilities to identify and extract the governing dynamics of a system beyond the attractor where they are sampled and constructed [23–26].

ML-techniques come as an inspiration to support the development of nonlinear-based new methodologies for tapping mode AFM. In detail, approaches based on neural networks are of interest because of their ability to distill physical knowledge from time series [27–29]. Among different variants, the quasi-recurrent neural network (QRNN) is found particularly effective to interpret complex nonlinear behaviors [30,31]. Of major importance, hidden states of a QRNN are promptly accessible and they incorporate information on how the network processes the input data [32]. In this work, we make use of a QRNN to analyze and predict occurrence of modal coupling in dynamic AFM. Our data-driven approach aims, after a preliminary full training, to work with limited amount of data, i.e. a few portions of single acquisition of oscillation as input. For this reason it can be easily integrated into the traditional controllers with minor modifications and without data buffering. The QRNN performs the complete characterization of the AFM dynamics and it grasps the effective activation of higher modes of vibration.

To show the application of QRNN in dynamic AFM, we first use it over synthetic datasets mimicking the tip-sample interaction in tapping AFM. Numerical simulations allow to promote the well-known typical internal resonances encountered in experiments. Indeed, dynamic AFM finds harmonics of its first excited resonant mode clashing with higher modes of vibration. It must be remarked that rectangular cantilevers used in the experiment, often see the ratio between the higher vibrational and the fundamental mode close to integer factors. Therefore, by tuning the nonlinear resonance frequency, the microcantilever undergoes internal resonance with activation of higher modes of vibration. The resulting mode coupling enhances the signal-to-noise ratio (SNR) of specific harmonics that are close to the interacting eigenmodes [14]. This enhancement in SNR can be harnessed to improve the nanoscale characterization techniques in multifrequency AFM (MF-AFM) as well as obtaining high resolution images of soft polymeric samples and biological materials using higher harmonics.

By making use of our preliminary knowledge on the expected modes, we examine the hidden layers of the neural networks. While detuning the excitation frequency, higher modes arise and the neural network units activate accordingly. Our goal is to determine if and how the interpretation of the hidden layer is employable as a filter to determine the dynamical status of the system.

Next, we apply the technique on experimental data in the presence of strong and weak tapping forces. We use the same trained network for the experimental data on different materials namely, silicon and mica. Despite dissimilar conditions in the tip-sample interaction, the dynamical response possesses common dynamical signatures over which the QRNN can be learnt. This permits us to recognize he same underlying nonlinear effects in conditions outside the training dataset. In terms of applicability, the QRNN greatly eases the signal interpretation in a variety of experiments, avoiding the need to collect the entire time trace. In a wider perspective, this approach is applicable to different nanomechanical systems and it could serve as an interpreter of complex nonlinear dynamics.

2. Results

2.1. Data-driven methodology

The concept of the developed identification methodology is illustrated in Fig. 1. We begin by training the QRNN with time domain data containing all the dynamical features necessary to untangle the underlying physics of interaction. The time series data can be either synthetic data coming from simulations, experimental data or a mixed ensemble of both types of data. Furthermore, the time series data is divided into a training data set and a validation data set. The algorithm is trained using only the training data set and once the training is completed the recurrent network is validated against an augmented data set containing both the training data as well as the unseen validation data set (prediction box in Fig. 1(b)). This allows for correcting any overfitting on the training data set and it further permits to check the accuracy of the prediction on data previously not seen by the algorithm. The QRNN implements convolutional layers that elaborate the data forward in time while recurrent relations are applied in the pooling layers (see Appendix A.2 for details). Pooling functions activate neurons regardless past outputs of other neurons. This structure avoids deep coupling interaction between neurons and it permits the interpretation of the network. Finally, we analyze the hidden layers of the network that successfully captures the dynamics of the system, (Fig. 1(c)). In particular, we look for activation of hidden units in connection with nonlinear dynamical features in order to ascertain the influence of higher modes of vibration. It is
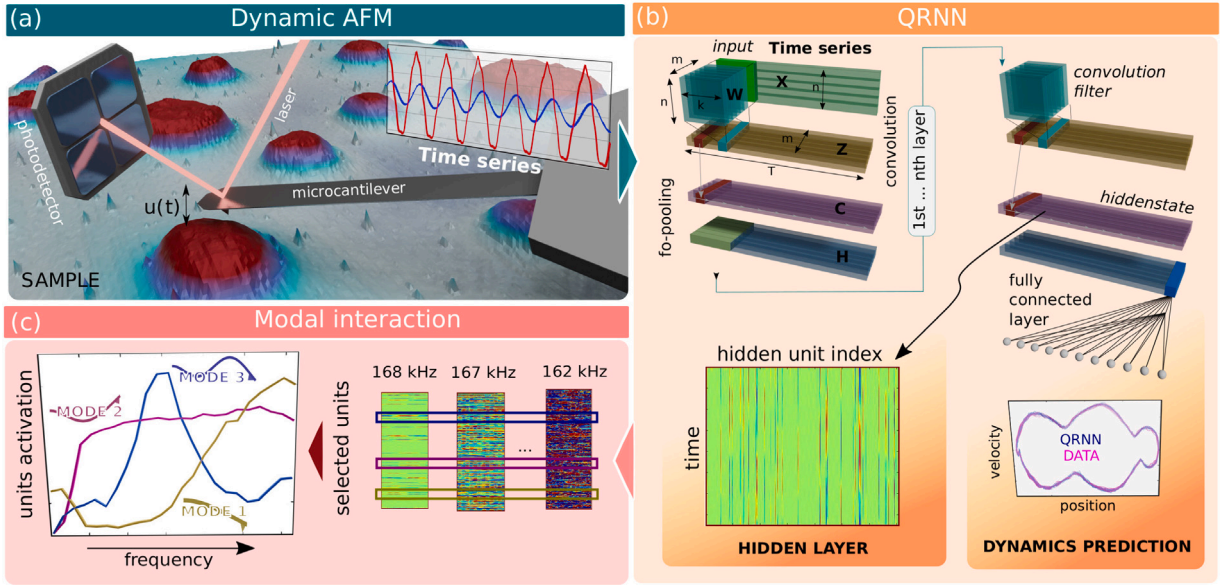
Fig. 1. Schematic of the identification process. (a) Sensing mechanics of an dynamic AFM system. The photodetector captures the deviations in raw deflection of the microcantilever interacting with the sample. (b) The state vector channels are used as inputs in the data-driven identification/prediction algorithm. Details regarding the QRNN algorithm are reported in Appendix A.2. (c) The QRNN estimates the modal interaction in the AFM dynamics. Hidden states in the QRNN layers detect mode activation; whereas, the color map indicates how strong units are activated.

worth mentioning that the training is computationally cumbersome and would benefit from reducing the dimension of the training data set such that it contains a majority of the nonlinear features in the prediction phase. Nevertheless, the main advantage of a thorough training is that once the dynamical features are captured, the network can be deployed over the testing data set without any additional operations and the network will still maintain its ability to predict the previously learned dynamical signatures.

2.2. Formulation and numerical results

We begin with a study on synthetic data sets to present the mechanisms of the proposed data-driven methodology. A theoretical model based on a non-smooth and nonlinear three-degree of freedom system is used to understand the nature of the mode coupling in tapping mode AFM. The AFM cantilever is modeled as a dynamical system using linear Euler–Bernoulli beam theory. Next, the cantilever deflection is projected onto its linear eigenmodes (computed near free air resonance) to obtain a system of ordinary differential equations via the Galerkin approach [33]

$$\ddot{q}_i + D_i(z)\dot{q}_i + K_i q_i = -C_i - F_{ts,i}(z) + B_i \Omega^2 y \sin(\Omega\tau). \tag{1}$$

Here, q_i $(i = 1, 2, \ldots, N)$ are the generalized coordinates of the AFM modes used to reconstruct the tip displacement $z = \sum_i^N q_i + y\sin(\Omega\tau)$. The equation is made dimensionless with respect to the equilibrium gap width (η^*) and the fundamental free-vibration frequency ($\omega_0 = 2\pi f_0$) of the cantilever. The amplitude of the dither piezo is given by y and the dotted quantities represent derivatives with respect to the re-scaled time τ ($\tau = \omega_0 t$). We consider a piecewise model for modal damping $D_i(z)$ which accounts for the different dissipation mechanisms i.e when the tip is not in contact with the sample (D_i^{att}) versus when it is in contact with the sample (D_i^{rep}) [34]. Furthermore, the coefficients K_i, C_i, and B_i are the normalized modal stiffness, static deflection, and mode participation factor, respectively. In Eq. (1), the tip-sample interaction $F_{ts}(z)$ comprises long range nonlinear Van der Waals (VdW) and Derjaguin–Muller–Toporov (DMT) contact forces [34,35]. The tip–surface interaction is purely attractive when the separation distance z is larger than the intermolecular distance (a_0). Otherwise, the interaction is governed by the contact mechanics. Non-smoothness of the interaction force provides a path for energy transfer between different modes of vibrations [14,18].

Finally, the discretized Eq. (1) is truncated to $N = 3$ and simulated using a pseudo arc-length continuation technique suited for hybrid dynamical systems [36]. Fig. 2 showcases the sample indentation in the contact region as a function of the excitation frequency, i.e. how much the tip penetrates the sample. The response highlights a strong hardening effect. As a matter of fact the sample acts as a physical wall for the impacting tip. The growth of the amplitude response is constrained leading to the so-called "amplitude-saturation". The model parameters are tweaked to produce 6:1 and 17:1 internal resonance of the fundamental mode with the second and third mode of vibration, respectively since these specific internal resonance are the most commonly observed dynamical phenomena in experiments [19,37,38].

Fig. 2 shows the warping of the frequency response branch due to modal interactions and can be exploited for designing effective AFM characterization techniques [14]. Fundamentally, this phenomenon is related to energy transfer induced by closeness of the
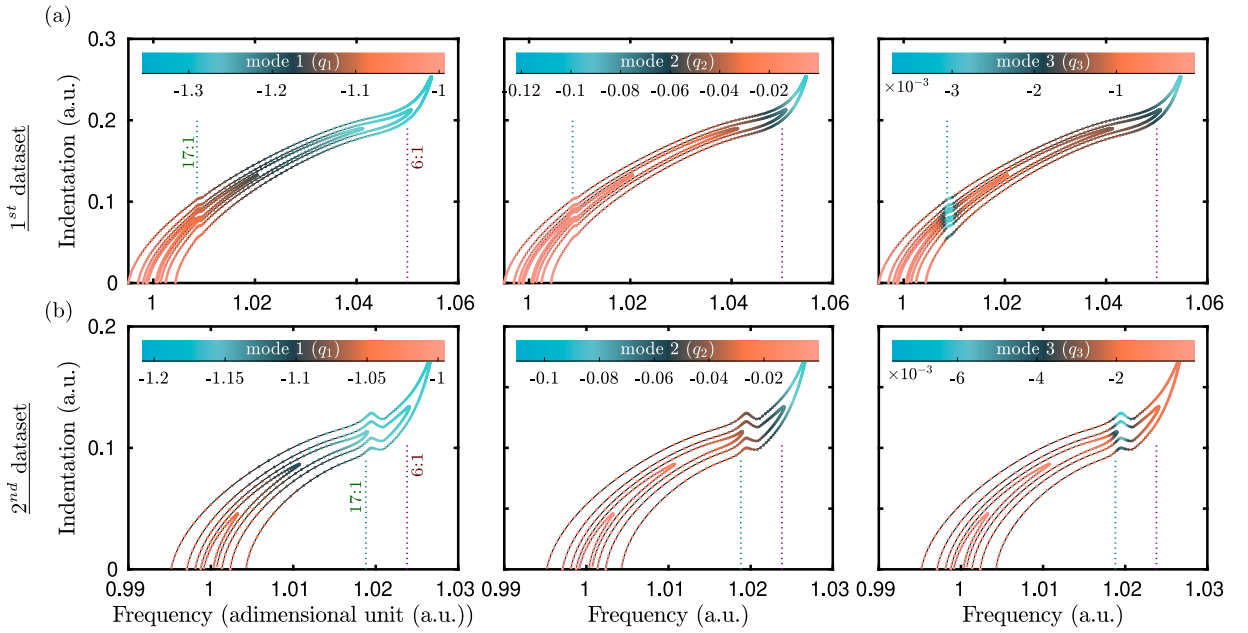
(a)

(b)

Fig. 2. Simulated nonlinear dynamic response in the repulsive region obtained with the three-mode model of Eq. (1). (a) 1st dataset (first raw): $y = \{0.0024, 0.0026, 0.0031, 0.0041, 0.0063\}$, $K_2 = 39.739$, $K_3 = 294$. (b) 2nd dataset (second raw): $y = \{0.0023, 0.0025, 0.003, 0.004, 0.0062\}$, $K_2 = 37.739$, $K_3 = 300$. For each dataset three subplots show with a color gradient the ith mode contribution q_i. Simulation parameters are provided in Supplemental Information SII.1 and SII.2.

higher modes to specific higher harmonics such as the 6th and 17th harmonic of the AFM cantilever [14]. Here, we use color gradients to highlight the contribution of each of the three modes to the total deflection of the cantilever. Fig. 2 shows two data sets with different modes coupling conditions. In Fig. 2(a) the resonance of the second and third mode are kept well separated; whereas they almost collide in the simulations of Fig. 2(b).

In the next step, we employ our QRNN algorithm made up of three layers to capture the dynamics of the AFM as shown in Fig. 3. The implicit details necessary to replicate the training reported in this article are provided in Appendix A.3. It is interesting to note that our data-driven approach accurately replicates the complex non-smooth dynamics of the multi-modal AFM system. Furthermore, only a few selected sub-orbits highlighted as dotted black lines in Fig. 2(a) and (d) are used for training the QRNN framework. This further emphasizes the importance of having a data set with all the necessary dynamical features during the training stage of the data-driven modeling. Overlooking a few fundamental orbits would make the network unable to recognize features related to the modes activation (for details, see Supplemental Information SII.3).

The high fidelity reconstruction of the oscillatory orbits suggests that the network successfully captures the properties of the system. This is shown in Fig. 3(a) and (d). It is indeed this excellent agreement in the orbits, with all the detailed features (Fig. 3(b) and (e) for the 1st/2nd dataset, respectively), that grants for a subsequent analysis of the recurrent network. In particular, the hidden units of the third layer are inspected to recognize patterns arising due to the evolution of the higher modes of vibration. The selected hidden units are compared to the mode activation in Fig. 3(c) and (f). These hidden units react in accordance with the variation in contribution of higher order modes to the overall cantilever oscillation. (Supplemental Information SII.4 reports an extended collection of units). The step by step process for analysis and selection of these hidden units will be detailed out in Section 2.3.

2.3. Experimental observation of mode- coupling in dynamic AFM

In order to identify the influence of higher modes on the cantilever oscillations, we begin by examining the experimental data obtained with a standard silicon cantilever on a flat silicon sample (the experimental procedure is detailed in Appendix A.1). The experimental frequency response for an excitation amplitude of $0.016V$ is shown in Fig. 4(a) and (b), whereas its time evolution in the phase space is shown in Fig. 4(c). From Fig. 4(a), we observe that as the excitation frequency increases during a forward sweep, the resonance curve showcases a strong bending toward the right side of the resonance (spring hardening) due to the repulsive forces between the tip and the sample. This nonlinear behavior leads to a large hysteretic region wherein the amplitude depends on the direction of the sweep.

Furthermore, the amplitude-saturated branch in Fig. 4(b) highlights a wave-like behavior with two curvatures. The resulting concave valley, referred to as the "sweet spot", is due to the presence of a particular dynamical regime that is able to minimize the sample indentation [14]. This sweet spot is a direct consequence of a 6:1 internal resonance and manifests itself as distortions in the
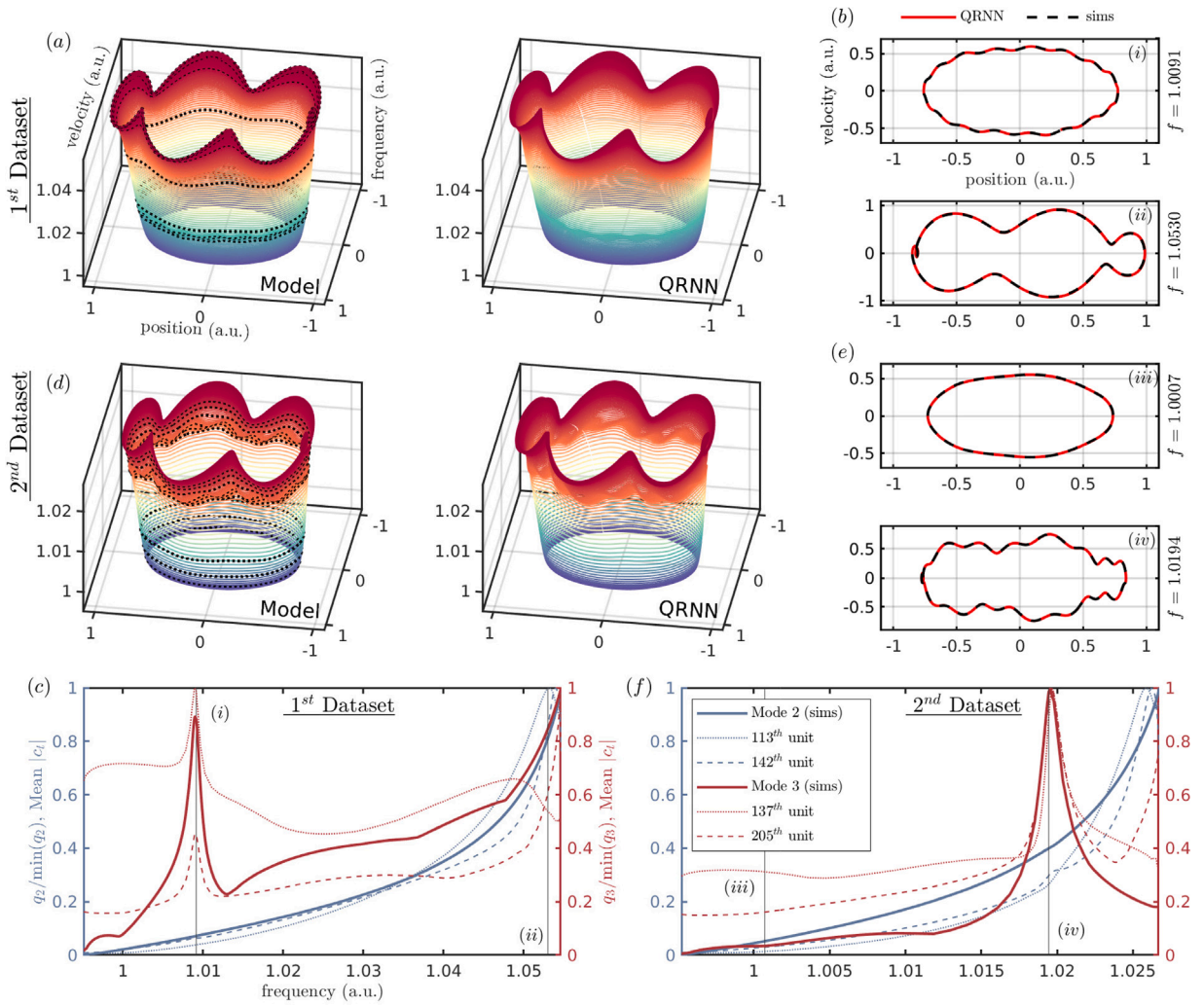
Fig. 3. Quasi-recurrent neural network prediction and analysis of the AFM nonlinear oscillations simulated with the three-mode model of Eq. (1). Results in (a)–(c)/(d)–(f) are for the 1st/2nd dataset of Fig. 2, $y = 0.0063$ and 0.0062, respectively. Subplots (b) and (e) show direct comparison for a few orbits from (a) and (d). In subplots (a) and (d) the dashed orbits are those selected for the neural network training. Subplots (c) and (f) show the trend of the higher order generalized coordinates $q_{2,3}$ with respect to the excitation frequency. In the same plot selected hidden units evolution are reported to highlight similar activation paths..

phase space trajectory of the cantilever. This is highlighted in Fig. 4(c), where the phase space orbit, initially circular, slowly warps as the excitation frequency is swept in the forward direction. The plot shows different wave-like regions associated with activation of higher modes of vibration.

Moreover, in contrast to the previous section, where the higher modes contribution can be directly accessed via the analytical model, in experiments, the activation of modes need to be deduced from the frequency spectra. This is shown in Fig. 4(d), where the surface and bar plots track the first three fundamental modes and their influence in correspondence to specific excitation frequencies. It must be noted that the second mode activates only near the frequency range of the amplitude-saturated branch and follows a nearly constant increment with f_{ex} before it drops down when jumping down from high to low amplitude branch (second bar plot of Fig. 4(d)). Whereas, the third mode shows a Gaussian-like behavior with respect to the excitation frequency (third bar plot) indicating selective sensitivity over a specific excitation frequency range. However, repeating the above process for every pixel during scanning operation requires significant post-processing and is highly sensitive to the rate of acquisition since it dictates the resolution of the frequency domain analysis. Hence, for these reasons we implement the QRNN-based data-driven technique as an alternative to retrieve the mode coupling in an easy and computationally efficient manner.

2.4. Data-driven based prediction of higher order mode coupling in experiments

In order to disentangle the effects of higher order modes, first the experimental data is reshaped into a vector **X** that contains the displacement u of the cantilever and the velocity $\dot{u}$ obtained numerically by differentiation.
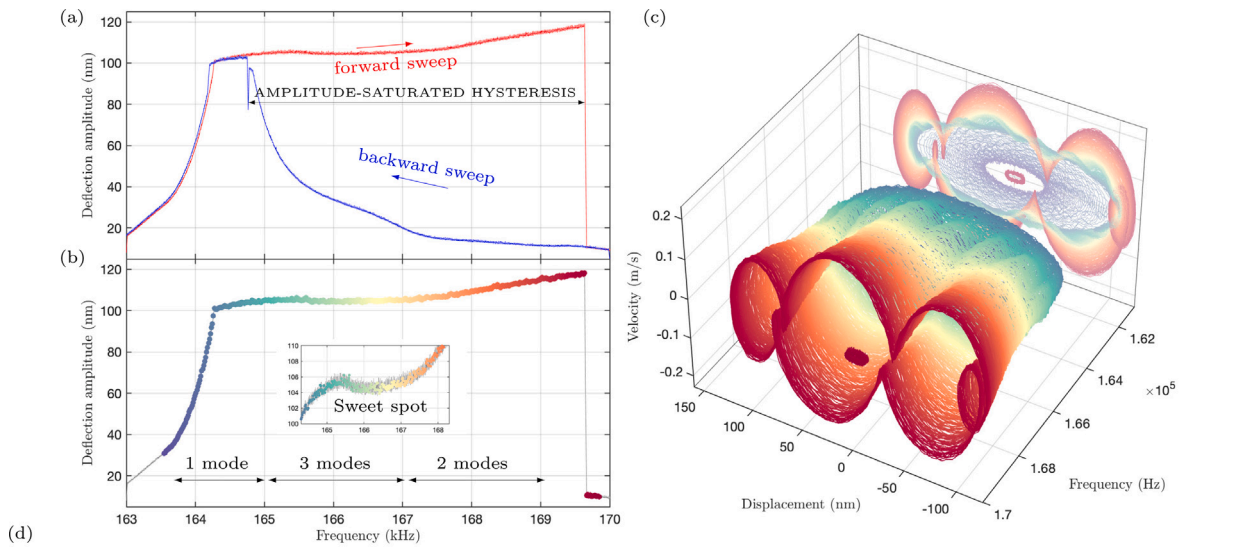
Fig. 4. Experimental nonlinear dynamic response and phase-space trajectories. (a) Experimental frequency-response curve obtained from the raw minimum deflection signal of the cantilever; the red and the blue curves represent the forward and reverse sweeps in the excitation frequency f_{ex}. (b) Detailed zoom on the upper branch of (a), in the inset the knee of the curve in the amplitude saturated region, i.e. "sweet spot" [14]. Colorcode is in accordance with subfigure (c). (c) Phase-space trajectories for $f_{ex} \in [164.1, 167.1]$ kHz showing the influence of higher eigenmodes in the cantilever oscillations. Color gradient is accordingly to subfigure (b). (d) Spectrum analysis of the experimental FFT normalized by the maximum peak value of the spectrum for different excitation frequencies. Darker colors mean higher amplitude in the frequency response.
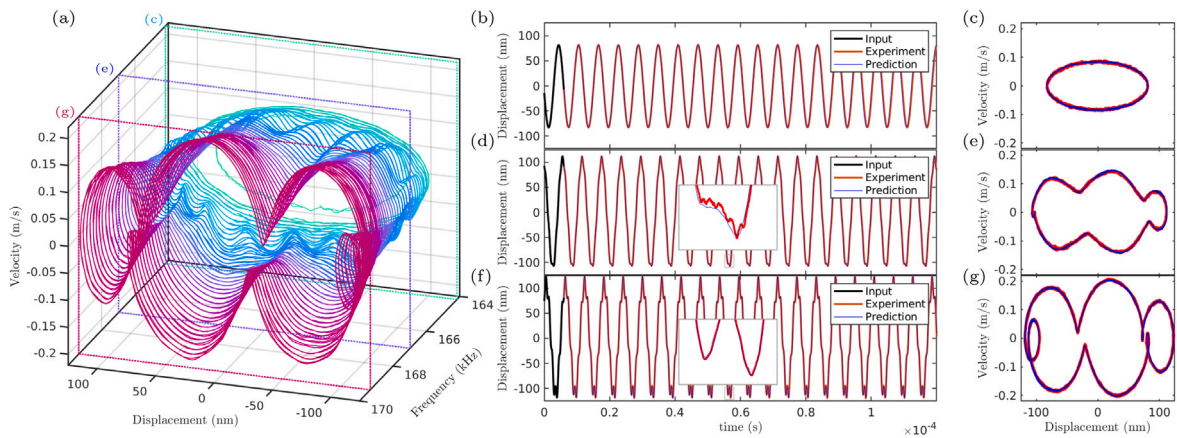

Fig. 5. Quasi-recurrent neural network prediction of the AFM nonlinear oscillations. (a) Evolution of the orbits. Color gradient from cyan to purple for an increasing excitation frequency $f_{ex} \in [164.1, 169.4]$. QRNN prediction (blue line) compared with the experimental data (red line) in time (subplots (b),(d),(f)) and in the phase-plane (subplots (c),(e),(g)). Black solid lines are the initial input data (a single oscillation period) for the QRNN which are obtained from the testing data. (b)–(c) Weak interaction at $f_{ex} = 164.175$ kHz, (d)–(e) Medium interaction at $f_{ex} = 166.976$ kHz, (f)–(g) Strong interaction at $f_{ex} = 169.356$ kHz.

Fig. 5 shows the AFM dynamics predicted by the QRNN in comparison with the actual experimental data. Estimation is based on one period (1500 points) and there is no training and cross validation as this applies only in the training stage. We visualize this prediction of the cantilever dynamics in the $u - \dot{u} - f_{ex}$ plane in Fig. 5(a). QRNN shows remarkably accurate prediction of the
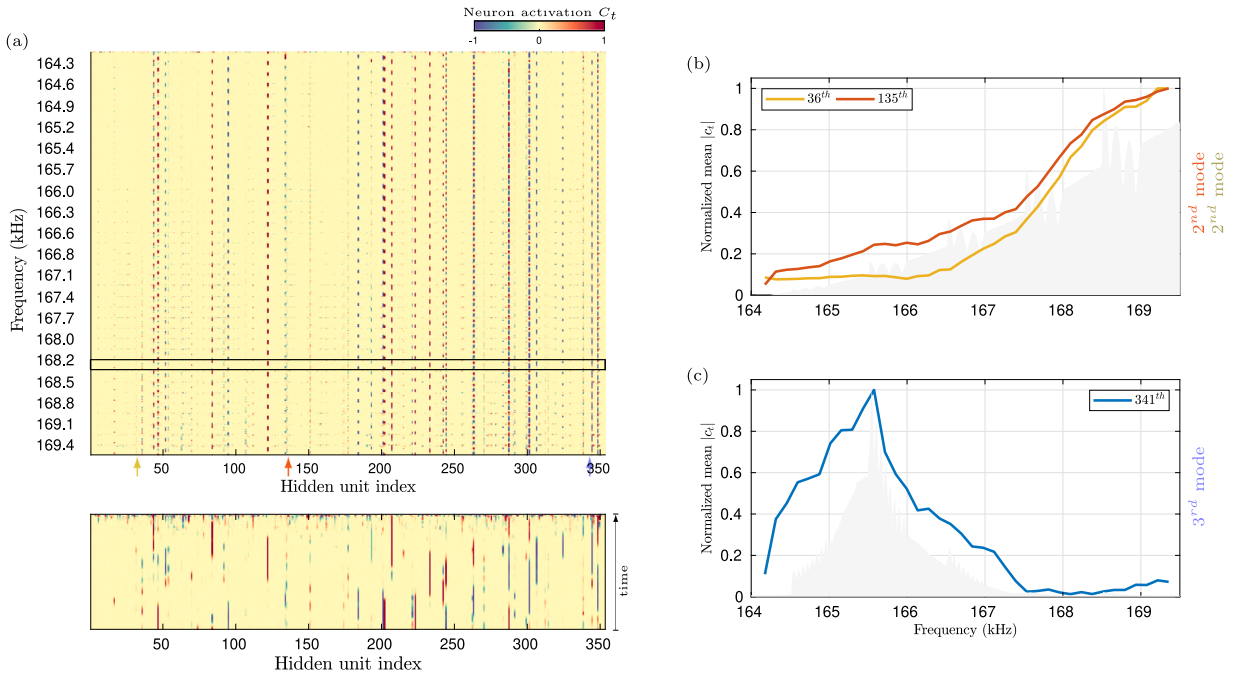
Fig. 6. Visualization of the hidden states of the quasi-recurrent neural network (QRNN). (a) Hidden states of all units for the third layer. Activation is visualized as surface plots where colors denote the activation of each hidden unit. Below, the zoom for $f_{ex} = 168.23$ kHz with the progress of the unit in time. (b)–(c) The neuron activation of selected individual hidden units. Average neuron activation value for $|c_t|$ grouped by its evolution with respect the excitation frequency.

underlying dynamics considering that no mathematical model nor any prior knowledge of the dynamical system were employed and the prediction purely stems from measured experimental data. The network begins by reconstructing the dynamics starting from the case of weak tip-sample interaction (Fig. 5(b) and (c)) and works its way up to strong intermodal coupling (Fig. 5(f) and (g)) where the presence of higher order modes warps the phase space trajectories with ripples appearing on the periphery of the orbit.

Since the dynamics predicted by the QRNN algorithm matches excellently with that of the experimental data, we now inspect the characteristics of the network that can correspond to specific dynamical fingerprints. In particular, we look for the underlying features of the network such as the highly activated hidden units of the QRNN network displaying correlation with activation the modes in the experimental data as in Fig. 4(d).

Let c_{t_n}, with $\|c_t\| \leq 1$ be the value of activation for the nth hidden unit in the third NN layer. The hidden state for a single layer comprises 352 hidden units. Their values are tracked for the entire range of excitation frequencies, i.e. $c_{t_n} = c_{t_n}(f_{ex})$. The condensed map of Fig. 6(a) gives an overall picture of the evolution of the c_{t_n} activation in the third NN layer. Each frequency row, from bottom to top, sees the variation of the unit as a function of time for a period T as illustrated for the zoomed frequency $f_{ex} = 168.23$ kHz at the bottom of Fig. 6(a). The visualization of activation values suggests several recurring patterns in the hidden states. It is worth analyzing the interesting triggering behavior of units with frequencies. We select the layout of highly activated units leading to motifs as in the spectral trend of Fig. 4(d). Strong activation of units associated with a rise of the second mode and third mode of vibration are reported in Fig. 6(b) and (c), respectively. Further units possess analogous behavior of those reported although they have a lower level of activation.

In the next step we confirm the match found in Fig. 6(b) and (c) between higher modes and hidden units evolution by analyzing cantilever's trajectories. This is shown in Fig. 7 where three dynamical scenarios are reconstructed, each representing a different degree of strength of intermodal coupling. Fig. 7(a)–(c) shows the predominance of the third mode; whereas, Fig. 7(d)–(f) displays a second mode weakly activated; and finally, Fig. 7(g)–(i) present strong mode interaction between the first and the second flexural mode. Classification of the motion can be inferred by the warping observed in the phase space, large smooth folds are hints of the second flexural mode (e.g. Fig. 7(d) and (g)) whereas crumpling is associated with the third mode being activated (Fig. 7(a)). This can be verified using numerical models and doing several FFT targeted for activation of higher order modes as reported in [14]. Nevertheless, this correlation can be formalized inspecting the activated units. The QRNN network advances forward in time, in parallel across multiple time steps and it builds the correlation of hidden units between different time steps. This property allows to check the hidden unit that responds to time feature and which feature repeats at specific time steps. Indeed, the activation of unit in time relates with the wrinkles of the orbit and it allows to determine their activation frequency (last row of Fig. 7). Such investigation could be of particular help when unaware of the actual modes coming into play, the network hints to generic vibrational components. Those have to be labeled accordingly to the reconstruction of the signal. This could be achieved via a signal reconstruction based on a projection over the manifold of specific units. Details of this extension are out of the scope of this work and left for future works.
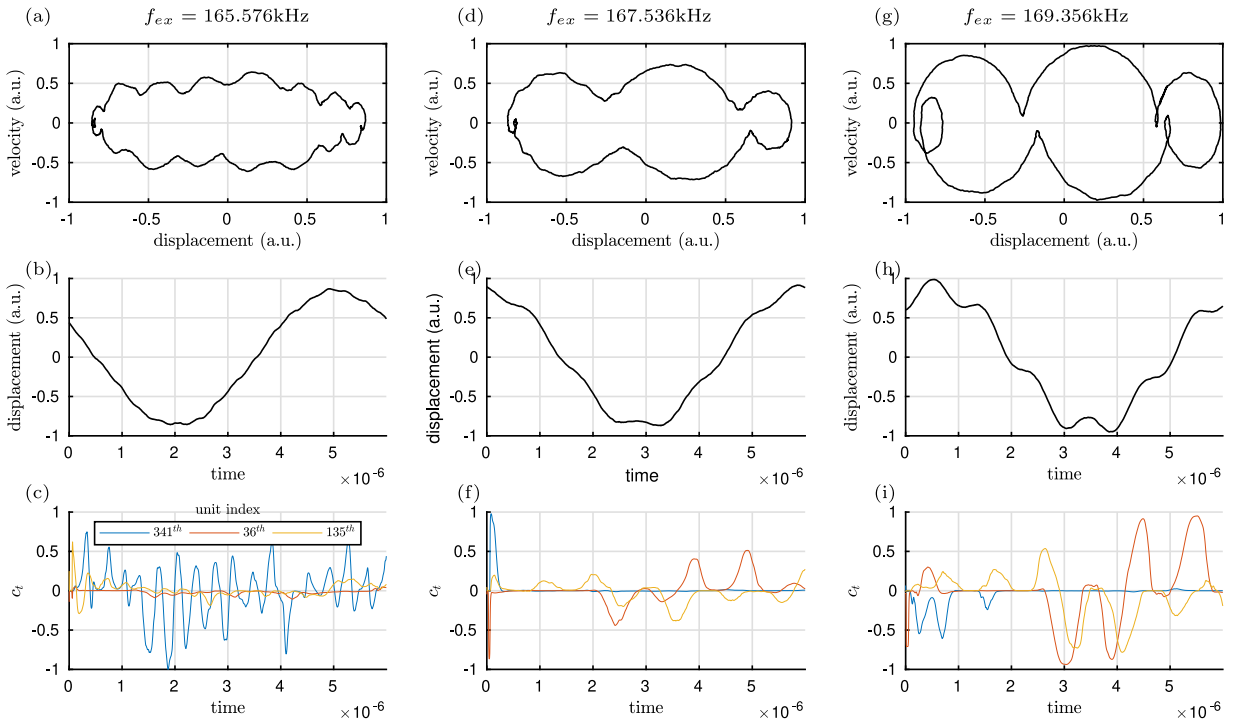
Fig. 7. Relation of the hidden states of the quasi-recurrent neural network with the emergence of mode coupling for three excitation frequencies: (a)–(c) $f_{ex} = 165.576$, (d)–(f) $f_{ex} = 167.536$, (g)–(i) $f_{ex} = 169.356$. Evidence of the response is shown in the phase space (a),(d),(g), time traces (b),(e),(h) and neuron activation (c),(f),(i) for the 36th, 43th and 135th hidden unit. We remark that the participation of other units are found to be of minor importance and only a few units govern the warping mechanism of the phase space. A similar observation holds true for other experimental data sets (see section Supplemental Information SI.1). Both subfigures (f) and (i) report confined regions of activation of the unit 341 (the one associated with the third mode of vibration). The presence of the third mode, even if minor, it is in agreement with the experimental findings of Fig. 4(d).

2.5. Extension of the QRNN prediction over additional AFM experiments

The aforerepresented approach is generalized over additional sets of experiments to prove a broader applicability and to verify its repeatability. We modify the experimental conditions, that results in different tip-sample interaction and, as a byproduct, new mixtures of information are coded into the AFM cantilever oscillation. In this section, we look at the performance of the previously trained QRNN on two additional experimental data sets .

In the first additional data set we use the same cantilever previously used (Fig. 4), however a different excitation amplitude varies the energy of the impact between tip and sample. In particular, we reduce the voltage applied at the dither from the 0.016 V of the training data set to 0.015 V. As a consequence of the reduced excitation amplitude, the AFM trajectory shows lower distortion. The orbits showcased in Fig. 8 present less warping than those in the case of Fig. 4. The indentation depth is also reduced and the sweet-spot region shrinks as shown in Fig. 8(a). Irrespective of the change in the interaction energy, the QRNN excellently reconstructs the phase space as revealed by the comparison with the experiments in Fig. 8(b) and (c).

In the second supplemental experiment a standard TAP190Al-G rectangular cantilever is used to probe a flat muscovite mica sample. Once again, the QRNN manages to maintain the high fidelity of the reconstruction as shown in Fig. 9. The excellent agreement of the prediction with respect to the experimental data indicates that the training of Section 2.4 was performed over a sufficient library of tip-sample interaction mechanisms. In other words, the recurrent network was successful in grasping all the dynamical features of different experiments without any additional training. In both additional experiments (different excitation amplitude and different material), the same hidden units are still correlated with the coupling of modes (see Figs. 8(d) and 9(d)). The trend of these hidden units are similar to that of Fig. 6(b) and (c). The corroboration of one trained network over different experiments stands as load-bearing requisite for practically integrate the data-driven approach with detection schemes based on nonlinear modes coupling.

3. Conclusion

In summary, we introduce a data-driven approach to investigate modal coupling in nanomechanical systems as alternative to traditional spectral analysis. We explore the capability of the QRNN to predict intermodal coupling in tapping mode AFM by using synthetic data sets obtained from simulating a non-smooth and nonlinear model. We show that the QRNN reconstructs the nonlinear
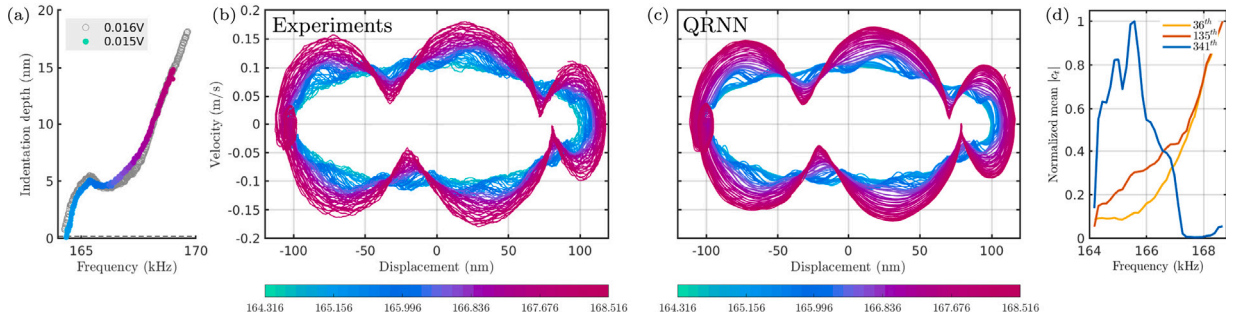
Fig. 8. Quasi-recurrent neural network prediction for the excitation amplitude A_{ex} = 0.015 V. (a) Indentation depth compared with the previous experimental conditions (A_{ex} = 0.016 V); (b) Experimental phase-space orbits; (c) Predicted phase-space orbits; (d) Average neuron activation of selected individual hidden units.
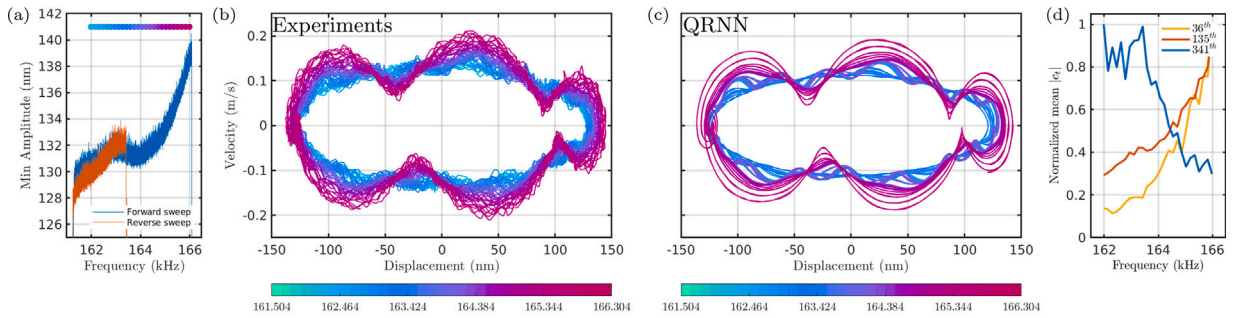

Fig. 9. Quasi-recurrent neural network prediction for a TAP190Al-G rectangular cantilever interacting with a flat Muscovite Mica sample. (a) Frequency response with the sweet spot; (b) Experimental phase-space orbits; (c) Predicted phase-space orbits; (d) Average neuron activation of selected individual hidden units.

dynamics of tip-sample interaction with high fidelity. In addition to the effectiveness of capturing the underlying dynamics of the system, the QRNN deciphers individual contribution of higher order modes. It is possible to reconstruct their variation over different regions of excitation frequency by analyzing the hidden units of the network. The insights gathered from the synthetic data set are used to train a three-layer QRNN to predict the experimental dynamics of a silicon cantilever interacting with a flat silicon sample. In particular, we studied the average neurons activation to correlate the response of the hidden units to dynamical patterns originating from higher order vibrational modes. Notwithstanding different cantilever-sample configurations with specific individual interaction mechanisms, there exist recurring features in the evolution of the cantilever orbit. A quasi-recurrent neural network trained on these fundamental patterns is able to grab the dynamics on multiple samples and different interaction conditions. This allows for a unique trained network to be a modal interaction sieve for different experimental conditions, e.g. soft/strong tapping or different tip/sample materials. For a wider applicability, it is advisable to perform the training with an augmented dataset with multiple intermixed tip-samples configurations each of which provides individual peculiar features.

Currently there is no universal technique to analyze mode coupling in dynamic AFM. Many studies incorporate multifrequency-AFM techniques to map nanomechanical properties of samples, e.g. polymeric, biological substances. However, only a few look into the opportunity for enhancing the sensitivity of the higher-order spectral components. In addition, internal resonance has been exploited by modifying the geometry of the cantilever with notches or holes or by adding a concentrated mass at specific locations on the cantilever. Our approach is meant to assist the choice of suitable dynamical conditions for dynamic AFM only by tuning the nonlinear resonance frequency. In this way the internal resonance can be triggered and activate the contribution of higher modes without needing specialized cantilevers and advance knowledge of cantilever dynamics. We believe the proposed data-driven approach can be utilized to guide the AFM sensing operation, by allowing to enhance the SNR of higher harmonics and by extension improve the accuracy of nanomechanical characterization, e.g. high resolution compositional contrast in multi-frequency AFM applications. Finally, given the generalized nature of the proposed methodology, the approach can be extended to different micro and nanomechanical systems to understand the hidden nonlinear dynamical interactions.

Declaration of competing interest

The authors declare that they have no known competing financial interests or personal relationships that could have appeared to influence the work reported in this paper.
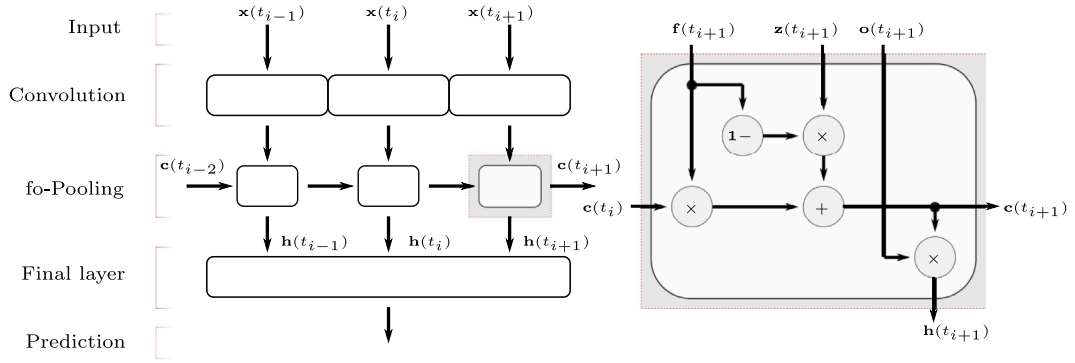
Fig. 10. Block diagram of a QRNN with the computation structure made of convolution and pooling layers. The pooling section implements recurrent relation, it gives $c(t_i)$ and $h(t_i)$ based the forget gate (f), candidate vector (z), and output gate (o). This operation depends only on $c(t_{i-1})$ from the previous time step.

Data availability

Data supporting the findings in this manuscript are available upon request.

Appendix A. Methods

A.1. Experimental procedure

The experiments are done using a commercial AFM system (JPK Nanowizard) and with commercially available cantilevers and samples.

The experimental data set is obtained by first holding the cantilever at a precise fixed distance from the sample while the dither piezo drive frequency is swept forward and backward around the resonance frequency at a constant excitation amplitude. The resulting cantilever oscillations are recorded at each frequency step directly from the photo-detector using an Field Programmable Gated Array (FPGA) from National Instruments with sampling frequency of 250 MHz. The operating conditions are comparable with that of the standard amplitude set-point ratios used during normal scanning operation in dynamic AFM [14]. The time series cannot be stored synchronously to an external hard drive while sweeping the excitation frequency due to low data transfer bandwidth and high-frequency dynamics. Thus data-buffering allows for a complete acquisition while storing the chunks of time series within the FPGA and intermittently transferring it to an external hard disk for further analysis. This represents a major drawback that makes real time analysis of the cantilever deflection extremely difficult. On the contrary, buffers are avoidable only by a massive reduction of each chunk duration length by recording a portion of each oscillation per each frequency; however this makes frequency-domain analysis challenging due to poor resolution.

A.2. Quasi-recurrent neural networks

Here we briefly summarizes the QRNN process to maintain the paper self contained. For additional details we encourage the reader toward the original paper of Connor et al. [27] and to the Supplemental Information in Yasuda et al. [30].

The structure of the QRNN with the succession of the layers is sketch in Fig. 1(b). The time series vector is $\mathbf{X} = \left[\mathbf{x}(t_1), \mathbf{x}(t_2) \dots \mathbf{x}(t_T)\right]$ with $\mathbf{x}(t_i) = \left[x_1(t_i), x_2(t_i) \dots x_n(t_i)\right]$. The sequence $\mathbf{Z} \in \mathbb{R}^{T \times m}$ is calculated with candidate vectors $\mathbf{z}(t_i)$ and where m is the number of hidden units in a layer. By using the convolutional filter banks $\mathbf{W}_{z,f,o} \in \mathbb{R}^{k \times n \times m}$ with filter width of k, then $\mathbf{Z} = \tanh\left(\mathbf{W}_z * \mathbf{X}\right)$, $\mathbf{F} = \sigma\left(\mathbf{W}_f * \mathbf{X}\right)$, $\mathbf{O} = \sigma\left(\mathbf{W}_o * \mathbf{X}\right)$ are calculated (σ is the sigmoid function, $*$ denotes a masked convolution along the time sequence). Convolutional layer $\mathbf{F}$ and $\mathbf{O}$ are composed of $\mathbf{f}(t_i)$ and $\mathbf{o}(t_i)$ respectively for the gates required for the pooling components. The pooling components are obtained with the *fo-pooling*: $\mathbf{c}_t = \mathbf{f}_t \odot \mathbf{c}_{t-1} + \left(1 - \mathbf{f}_t\right) \odot \mathbf{z}_t$ and $\mathbf{h}_t = \mathbf{o}_t \odot \mathbf{c}_t$ where $\odot$ is elementwise multiplication. Element-wise calculation in the pooling functions activate neurons regardless past outputs of other neurons in the same pooling layer. Block diagram for the QRNN is sketched in Fig. 10. This structure resolves the deep level of coupling interaction and the challenge to extract meaningful information about the effects of individual neurons. Thus, hidden states of a QRNN are promptly interpretable and they incorporate information on how the network process the input data. Convolutional layers elaborate data in parallel forward in time whereas recurrent relations are implemented within the pooling layers [32].

Table A.1
Parameters used in the QRNN.

Parameter	Symbol	Value
Batch dimension	b	25
Filter width	k	6
Epochs	e	100
Learning rate	l	10^{-3}
Decay rate	d	10

Fig. 11. Synthetic datasets: Training loss calculated from training and testing data sets over 100 training epochs.
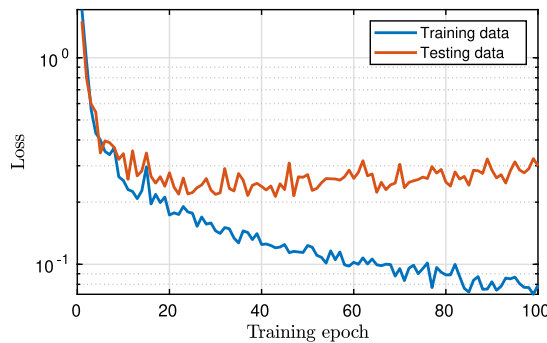

Fig. 12. Experimental datasets: Training loss calculated from training and testing data sets over 100 training epochs.

The network performs rolling cross-validation and prediction as follows. It approximates the underlying dynamics by advancing through the time series in steps of 6 μs which corresponds to an input chunk of $T = 1500$ steps. From $\mathbf{X} \in \mathfrak{R}^{1500 \times 2}$ the QRNN estimates the displacement and the velocity for the next 500 steps. Based on the predicted 500 steps and the last 1000 from the input data, another 500 time steps are forecasted. The routine goes on until a suitable prediction is evaluated.

A.3. Quasi-recurrent neural networks training

We train the QRNN selecting only a few orbits in the full frequency range (Supplemental Information SII.3). The QRNN training has been set up with the parameters in Table A.1. Training is optimized by using Adam optimization algorithm. Training loss is in Fig. 11 and Fig. 12 for the synthetic and experimental dataset, respectively. The Python code uses the 1.14 gpu version of the ML library TensorFlow. Additional details regarding the QRNN employed in this work can be found in [30].

Appendix B. Supplementary data

Supplementary material related to this article can be found online at https://doi.org/10.1016/j.ymssp.2022.109312.

References

[1] J.F. Rhoads, S.W. Shaw, K.L. Turner, Nonlinear dynamics and its applications in micro- and nanoresonators, J. Dyn. Syst. Meas. Control 132 (2010) 034001, http://dx.doi.org/10.1115/1.4001333.

[2] R. Lifshitz, M.C. Cross, Nonlinear dynamics of nanomechanical and micromechanical resonators, in: Reviews of Nonlinear Dynamics and Complexity, John Wiley & Sons, Ltd, 2008, pp. 1–52, Chap. 1 https://onlinelibrary.wiley.com/doi/abs/10.1002/9783527626359.ch1.

[3] Y. Tadokoro, H. Tanaka, Highly sensitive implementation of logic gates with a nonlinear nanomechanical resonator, Phys. Rev. Appl. 15 (2021) 024058, http://dx.doi.org/10.1103/PhysRevApplied.15.024058.

[4] S. Rips, I. Wilson-Rae, M.J. Hartmann, Nonlinear nanomechanical resonators for quantum optoelectromechanics, Phys. Rev. A 89 (2014) 013854, http://dx.doi.org/10.1103/PhysRevA.89.013854.

[5] M. Yuksel, E. Orhan, C. Yanik, A.B. Ari, A. Demir, M.S. Hanay, Nonlinear nanomechanical mass spectrometry at the single-nanoparticle level, Nano Lett. 19 (2019) 3583–3589, http://dx.doi.org/10.1021/acs.nanolett.9b00546.

[6] M. Serra-García, F. Pérez-Murano, A. San Paulo, Nonlinear detection mechanism in quantitative atomic force microscopy characterization of high-frequency nanoelectromechanical systems, Phys. Rev. B 85 (2012) 035433, http://dx.doi.org/10.1103/PhysRevB.85.035433.

[7] J. Chan, T.P.M. Alegre, A.H. Safavi-Naeini, J.T. Hill, A. Krause, S. Gröblacher, M. Aspelmeyer, O. Painter, Laser cooling of a nanomechanical oscillator into its quantum ground state, Nature 478 (2011) 89, http://dx.doi.org/10.1038/nature10461.

[8] A.P. Foster, J.K. Maguire, J.P. Bradley, T.P. Lyons, A.B. Krysa, A.M. Fox, M.S. Skolnick, L.R. Wilson, Tuning nonlinear mechanical mode coupling in GaAs nanowires using cross-section morphology control, Nano Lett. 16 (2016) 7414–7420, http://dx.doi.org/10.1021/acs.nanolett.6b02994, Nano Letters.

[9] D. Rugar, P. Grütter, Mechanical parametric amplification and thermomechanical noise squeezing, Phys. Rev. Lett. 67 (1991) 699, http://dx.doi.org/10.1103/PhysRevLett.67.699.

[10] R. Almog, S. Zaitsev, O. Shtempluck, E. Buks, Noise squeezing in a nanomechanical duffing resonator, Phys. Rev. Lett. 98 (2007) 078103, http://dx.doi.org/10.1103/PhysRevLett.98.078103.

[11] Y. Tadokoro, H. Tanaka, M.I. Dykman, Driven nonlinear nanomechanical resonators as digital signal detectors, Sci. Rep. 8 (2018) 11284, http://dx.doi.org/10.1038/s41598-018-29572-7.

[12] E. Buks, B. Yurke, Mass detection with a nonlinear nanomechanical resonator, Phys. Rev. E 74 (2006) 046619, http://dx.doi.org/10.1103/PhysRevE.74.046619.

[13] L. Tetard, A. Passian, T. Thundat, New modes for subsurface atomic force microscopy through nanomechanical coupling, Nature Nanotechnol. 5 (2010) 105–109, http://dx.doi.org/10.1038/nnano.2009.454.

[14] A. Chandrashekar, P. Belardinelli, S. Lenci, U. Staufer, F. Alijani, Mode coupling in dynamic atomic force microscopy, Phys. Rev. Appl. 15 (2021) 024013, http://dx.doi.org/10.1103/PhysRevApplied.15.024013.

[15] R. García, R. Magerle, R. Perez, Nanoscale compositional mapping with gentle forces, Nature Mater. 6 (2007) 405–411, http://dx.doi.org/10.1038/nmat1925.

[16] W.J. Venstra, H.J.R. Westra, H.S.J. van der Zant, Q-factor control of a microcantilever by mechanical sideband excitation, Appl. Phys. Lett. 99 (2011) 151904, http://dx.doi.org/10.1063/1.3650714.

[17] T. Dunn, J.-S. Wenzler, P. Mohanty, Anharmonic modal coupling in a bulk micromechanical resonator, Appl. Phys. Lett. 97 (2010) 123109, http://dx.doi.org/10.1063/1.3489423.

[18] A. Keşkekler, O. Shoshani, M. Lee, H.S.J. van der Zant, P.G. Steeneken, F. Alijani, Tuning nonlinear damping in graphene nanoresonators by parametric–direct internal resonance, Nature Commun. 12 (2021) 1099, http://dx.doi.org/10.1038/s41467-021-21334-w.

[19] R. Potekin, S. Dharmasena, D.M. McFarland, L.A. Bergman, A.F. Vakakis, H. Cho, Cantilever dynamics in higher-harmonic atomic force microscopy for enhanced material characterization, Int. J. Solids Struct. 110–111 (2017) 332–339, http://dx.doi.org/10.1016/j.ijsolstr.2016.11.013.

[20] H. Li, Y. Chen, L. Dai, Concentrated-mass cantilever enhances multiple harmonics in tapping-mode atomic force microscopy, Appl. Phys. Lett. 92 (2008) 151903, http://dx.doi.org/10.1063/1.2909535.

[21] A. Chandrashekar, P. Belardinelli, M. Bessa, U. Staufer, F. Alijani, Quantifying nanoscale forces using machine learning in dynamic atomic force microscopy, Nanoscale Adv. 4 (2022) 2134–2143, http://dx.doi.org/10.1039/D2NA00011C.

[22] J. Schmidt, M.R.G. Marques, S. Botti, M.A.L. Marques, Recent advances and applications of machine learning in solid-state materials science, Npj Comput. Mater. 5 (2019) 83, http://dx.doi.org/10.1038/s41524-019-0221-0.

[23] M. Schmidt, H. Lipson, Distilling free-form natural laws from experimental data, Science 324 (2009) 81–85, http://dx.doi.org/10.1126/science.1165893.

[24] S.-M. Udrescu, M. Tegmark, AI Feynman: A physics-inspired method for symbolic regression, Sci. Adv. 6 (2020) eaay2631, http://dx.doi.org/10.1126/sciadv.aay2631.

[25] K. Champion, P. Zheng, A.Y. Aravkin, S.L. Brunton, J.N. Kutz, A unified sparse optimization framework to learn parsimonious physics-informed models from data, IEEE Access 8 (2020) 169259–169271, http://dx.doi.org/10.1109/ACCESS.2020.3023625.

[26] P. Müller, S. Abuhattum, S. Möllmert, E. Ulbricht, A.V. Taubenberger, J. Guck, Nanite: using machine learning to assess the quality of atomic force microscopy-enabled nano-indentation data, BMC Bioinformatics 20 (2019) 465, http://dx.doi.org/10.1186/s12859-019-3010-3.

[27] J.T. Connor, R.D. Martin, L.E. Atlas, Recurrent neural networks and robust time series prediction, IEEE Trans. Neural Netw. 5 (1994) 240–254, http://dx.doi.org/10.1109/72.279188.

[28] I. Goodfellow, Y. Bengio, A. Courville, Deep Learning, in: Adaptive Computation and Machine Learning series, MIT Press, 2016.

[29] M. Raissi, P. Perdikaris, G.E. Karniadakis, Multistep neural networks for data-driven discovery of nonlinear dynamical systems, 2018, arXiv:1801.01236 [math.DS].

[30] H. Yasuda, K. Yamaguchi, Y. Miyazawa, R. Wiebe, J.R. Raney, J. Yang, Data-driven prediction and analysis of chaotic origami dynamics, Commun. Phys. 3 (2020) 168, http://dx.doi.org/10.1038/s42005-020-00431-0.

[31] Z.Y. Wan, P. Vlachas, P. Koumoutsakos, T. Sapsis, Data-assisted reduced-order modeling of extreme events in complex dynamical systems, Plos one 13 (2018) 1–22, http://dx.doi.org/10.1371/journal.pone.0197704.

[32] J. Bradbury, S. Merity, C. Xiong, R. Socher, Quasi-recurrent neural networks, 2016, arXiv:1611.01576 [cs.NE].

[33] A. Chandrashekar, P. Belardinelli, U. Staufer, F. Alijani, Robustness of attractors in tapping mode atomic force microscopy, Nonlinear Dynam. 97 (2019) 1137–1158, http://dx.doi.org/10.1007/s11071-019-05037-y.

[34] S. Lee, S. Howell, A. Raman, R. Reifenberger, Nonlinear dynamic perspectives on dynamic force microscopy, Ultramicroscopy 97 (2003) 185–198, http://dx.doi.org/10.1016/S0304-3991(03)00043-3.

[35] R. García, A. San Paulo, Attractive and repulsive tip-sample interaction regimes in tapping-mode atomic force microscopy, Phys. Rev. B 60 (1999) 4961–4967, http://dx.doi.org/10.1103/PhysRevB.60.4961.

[36] H. Dankowicz, F. Schilder, Recipes for Continuation, Society for Industrial and Applied Mathematics, Philadelphia, PA, 2013, https://epubs.siam.org/doi/abs/10.1137/1.9781611972573.

[37] O. Sahin, S. Magonov, C. Su, C.F. Quate, O. Solgaard, An atomic force microscope tip designed to measure time-varying nanomechanical forces, Nature Nanotechnol. 2 (2007) 507, http://dx.doi.org/10.1038/nnano.2007.226.

[38] A. Keyvani, H. Sadeghian, M.S. Tamer, J.F.L. Goosen, F. van Keulen, Minimizing tip-sample forces and enhancing sensitivity in atomic force microscopy with dynamically compliant cantilevers, J. Appl. Phys. 121 (2017) 244505, http://dx.doi.org/10.1063/1.4990276.